ACS APPLIED OPTICAL MATERIALS

Editors' Choice
Open Access

pubs.acs.org/acsaom

Article

Deep Learning-Optimized, Fabrication Error-Tolerant Photonic Crystal Nanobeam Cavities for Scalable On-Chip Diamond Quantum Systems

Sander van Haagen,* Salahuddin Nur, and Ryoichi Ishihara

Cite This: https://doi.org/10.1021/acsaom.5c00060

Read Online

ACCESS | Metrics & More | Article Recommendations | Supporting Information

ABSTRACT: Cavity-enhanced diamond color center qubits can be initialized, manipulated, entangled, and read individually with high fidelity, which makes them ideal for large-scale, modular quantum computers, quantum networks, and distributed quantum sensing systems. However, diamond's unique material properties pose significant challenges in manufacturing nanophotonic devices, leading to fabrication-induced structural imperfections and inaccuracies in defect implantation, which hinder reproducibility, degrade optical properties and compromise the spatial coupling of color centers to small mode-volume cavities. A cavity design tolerant to fabrication imperfections—such as surface roughness, sidewall slant, and nonoptimal emitter positioning—can improve coupling efficiency while simplifying fabrication. To address this challenge, a deep learning-based optimization methodology is developed to enhance the fabrication error tolerance of nanophotonic devices. Convolutional neural networks (CNNs) are applied to promising designs, such as L2 and fishbone nanobeam cavities, predicting *Q*-factors at least one-million times faster than traditional finite-difference time-domain (FDTD) simulations, enabling efficient optimization of complex, high-dimensional parameter spaces. The CNNs achieve prediction errors below 3.99% and correlation coefficients up to 0.988. Optimized structures demonstrate a 52% reduction in *Q*-factor degradation, achieving quality factors of 5×10^4 under real-world conditions and a 2-fold expansion in field distribution, enabling efficient coupling of nonoptimally positioned emitters. Compared to previous deep-learning optimization methods, this approach achieves twice the *Q*-factor performance in the presence of fabrication errors, significantly enhancing device robustness. Hence, this methodology enables scalable, high-yield manufacturing of robust nanophotonic devices, including the cavity-enhanced diamond quantum systems developed in this study.

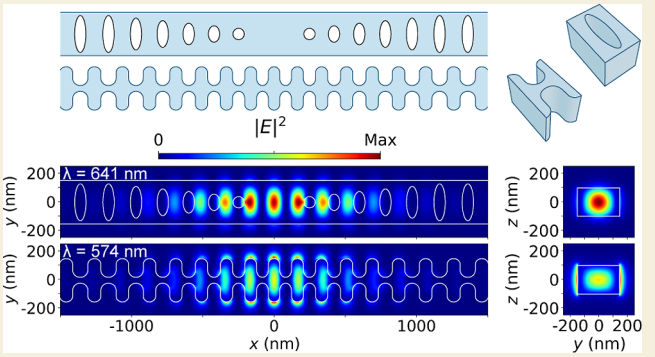

KEYWORDS: *deep-learning optimization, nanophotonics, fabrication-error tolerance, photonic crystals, nanocavities, diamond quantum systems, color centers, cavity quantum electrodynamics*

1. INTRODUCTION

Crystallographic defects in diamond known as color centers, such as nitrogen-vacancy (NV) centers and group IV defects (SiV, GeV, SnV and PbV centers), exhibit unique spin properties that make them promising building blocks for scalable and on-chip integrated quantum systems, including on-chip modular quantum computers,[1] distributed quantum sensors[2] and secure quantum networks.[3] This promise is attributed to their host's solid-state characteristics, which enable the implementation of large-scale fabrication processes. Additionally, color centers in diamond have demonstrated the capability for initialization, manipulation, entanglement, and readout of individual spin-qubits with long coherence times and high fidelity.[4−7]

The prospects of deploying color centers in diamond for solid-state quantum applications have driven the growth of diamond photonics. Photons serve as an effective medium for information transfer between qubits due to their fast propagation speed and weak interaction with the surrounding medium. Coherent spin-photon coupling emerges as the most promising approach for entangling such qubits, offering robust entanglement over extended distances.[8] However, to fully leverage the potential of color centers in diamond, it is essential to enhance the zero-phonon line (ZPL) and thereby increase coherent light emission.

Received: February 11, 2025
Revised: March 17, 2025
Accepted: March 24, 2025

Table 1. Table Comparing the Performance of Different Fabricated Visible Wavelength, Suspended Diamond Nanocavities[a]

Cavity type	Unit cell	Wavelength (nm)	Q-factor	Mode volume $\left(\frac{\lambda}{n}\right)^3$	Purcell factor	Method	Reference
1D							
Circular holes		737	1.83×10^5 (10^{6*})	0.5*	13	Thin film	Ding (2024)[20]
Sawfish		639	3825 (10^{6*})	0.8*	46*	Quasi-isotropic etching	Pregnolato (2024)[16,47]
Circular holes		618	1.1×10^4 ($6 \times 10^{5*}$)	0.42*	12	Quasi-isotropic etching	Kuruma (2021)[17]
Rectangular holes		620	2800 ($2 \times 10^{5*}$)	2.8*	N/A	Thin film	Regan (2021)[21]
Rectangular holes		775	8400 ($2 \times 10^{5*}$)	2.8*	N/A	Thin film	Regan (2021)[21]
Circular holes		617	2135 ($2 \times 10^{5*}$)	0.56*	25	Quasi-isotropic etching	Rugar (2021)[18]
Elliptical holes		737	2×10^4 ($5 \times 10^{5*}$)	0.5*	N/A	Angled etching	Bhaskar (2020)[14,15]
Circular holes		637	1.4×10^4 (10^{6*})	N/A	N/A	Quasi-isotropic etching	Mouradian (2017)[19]
Circular holes		660	2.4×10^4 ($2.7 \times 10^{5*}$)	0.47*	20	Thin film	Lee (2014)[22]
2D							
Circular holes		746	1.6×10^5 ($7.6 \times 10^{5*}$)	2.18*	N/A	Thin film	Ding (2024)[20]
Circular holes		645	8000 ($3.2 \times 10^{5*}$)	0.35*	1.224	Thin film	Jung (2019)[23]

[a]All values denoted with a "*" are simulated measures.

Cavity quantum electrodynamics (cQED) offers a route to achieve this, as on-chip integrated optical resonators can act as interfaces that enhance emission into the ZPL.[9,10] This enhancement, known as Purcell enhancement,[11] enables coherent coupling between the emitted light and the spin state of the spin-qubits, facilitating the possibility for on-chip quantum information processing tasks.

One candidate of such optical resonators are photonic crystal (PhC) nanocavities. These cavities trap light by introducing defects in the periodicity of PhC lattices.[12] Their demonstrated ability to achieve high quality factors (Q-factors) and small mode volumes at the ZPL results in large Purcell factors (see Supporting Information A). These nanocavities can vary in terms of unit cell structure, PhC defects, and dimensionality, leading to a diverse range of design options, design parameters and optical characteristics (see Table 1). However, diamond's extreme hardness and chemical stability present significant challenges for precise nanofabrication of such nanocavities, often leading to fabrication imperfections that degrade the performance of diamond nanophotonic devices. Addressing these challenges is critical for fully realizing the potential of diamond-based solid-state quantum technologies.

The most promising PhC nanocavities for scalable on-chip diamond quantum systems are 1D PhC nanocavities, also known as nanobeam cavities.[13] These cavities are characterized by periodic perturbations applied to a waveguide. They feature two Bragg mirrors positioned on either side of the resonant cavity. The cavity itself is typically formed by changing the distance between the two perturbations at the boundaries of the cavity region. These photonic structures are smaller than other 2D nanocavities, making them easier to fabricate using available techniques such as angled etching,[14,15] quasi-isotropic etching,[16−19] or diamond film thinning[20−23] (see Table 1). Additionally, their compact size is practical for scalable on-chip integration. However, fabricating these devices from diamond remains challenging and their performance is still highly susceptible to unavoidable fabrication imperfections. Table 1 shows that the experimentally determined Q-factors are generally more than an order of magnitude lower than the simulated Q-factors, primarily due to fabrication imperfections.

Hence, this work aims to address these fabrication challenges by developing an optimization methodology that enhances the tolerance of nanophotonic structures to common imperfections. More specifically, this study leverages deep learning (DL) techniques to optimize nanocavity designs for robustness against fabrication-induced imperfections while maintaining their optical performance metrics, such as high Q-factors and small mode volumes. This approach enables the creation of more resilient diamond nanocavities, which are critical for scalable, on-chip quantum technologies.

Standard nanocavity design and optimization are facilitated by finite-difference time-domain (FDTD) simulations, which can compute the propagation of light in both the spatial and temporal domains. While these simulations offer high accuracy without relying on theoretical approximations, they demand significant computational resources due to their intensive grid-based numerical method.[24] Previous optimization strategies have relied on techniques such as leaky mode visualization,[25,26] Gaussian envelope approaches,[27−29] and genetic algorithms.[30,31] These methods, whether trial-and-error or gradient-based, are often slow when dealing with large design parameter spaces like those encountered when optimizing nanobeam cavities.[32−40]

Recently, DL has emerged as an efficient alternative to computationally intensive methods based solely on FDTD simulations. Neural networks (NNs) acting as surrogate models can replace FDTD simulations, predicting optical properties at least one-million times faster and thereby enabling the inverse design of complex photonic structures.[41,42] DL-based methods have achieved high accuracy in predicting key metrics of PhC nanocavities, such as Q-factor

https://doi.org/10.1021/acsaom.5c00060
ACS Appl. Opt. Mater. XXXX, XXX, XXX−XXX

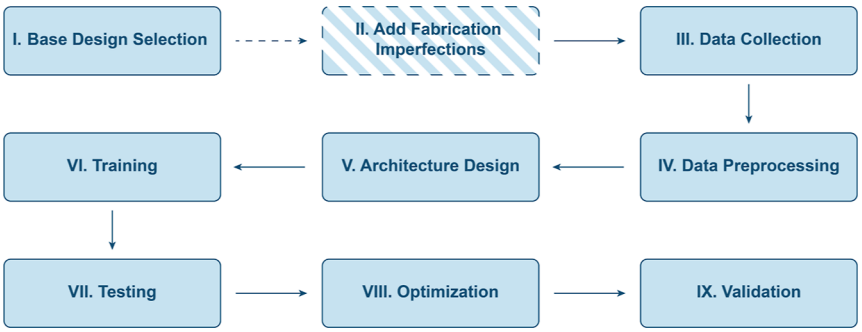

Figure 1. A flowchart illustrating the process for optimizing nanocavity designs using DL, highlighting the additional step introduced in this study.

and mode volume, utilizing a range of NN architectures, including feed-forward neural networks (FNNs),[32−34] convolutional neural networks (CNNs),[35−38] transformers,[39] and reinforcement learning (RL) models.[40] However, these previous efforts focused on materials that are more accessible for fabrication, whereas diamond's extreme material properties introduce additional challenges. As a result, unlike prior work that focused solely on high *Q*-factors, this study prioritizes optimization efforts to enhance tolerance to fabrication errors, ensuring robust device performance and thereby reducing the gap between simulated and experimentally obtained *Q*-factors (see Table 1).

This article focuses on optimizing the fabrication error tolerance of two base cavity designs, the L2 nanobeam and the fishbone nanobeam, chosen for their inherent resilience against two specific challenges. First, spin-qubits are susceptible to electric field fluctuations from charge variations, such as those occurring at nearby surfaces. Second, the defect implantation process can suffer from spatial inaccuracies, which degrade the spatial-spectral coupling between the emitter and the cavity mode.[43,44] These base designs allow for large cavity regions, which helps counteract these issues by increasing the emitter's distance from nearby surfaces and distributing the mode more broadly at the defect implantation site.

Three scenarios are compared for each base design, showcasing the proposed optimization technique. The two nanobeam base designs are each optimized under ideal conditions (no fabrication imperfections), against surface roughness,[45] and against sidewall slant.[46] These imperfections are common when fabricating such devices, even from thin film diamond, which is the most scalable fabrication technique among the three previously mentioned. A comparison of the simulated optical properties of ideally optimized nanobeam cavities with those optimized for fabrication error tolerance will reveal whether the latter perform better while suffering from these uncontrollable imperfections.

In summary, the development of fabrication error-tolerant diamond nanobeam cavities represents a critical step toward the realization of scalable quantum systems. This research leverages DL techniques to optimize the design of two promising diamond nanobeam cavities, addressing challenges posed by fabrication imperfections. By doing so, it aims to advance the practical integration of color centers in diamond for quantum information processing and quantum network applications. While the methodology was demonstrated on diamond nanobeam cavities, its applicability extends to the design of other fabrication error-tolerant nanophotonic structures, making it a system-agnostic approach.

2. METHODOLOGY

Previous work on optimizing nanocavities with DL, involving eight fundamental steps, primarily focuses on simulating extreme high *Q*-factors.[32−34,37,38] This research extends and enhances this approach by integrating a comprehensive evaluation of fabrication tolerances, ensuring robust optimization that addresses real-world fabrication challenges. The nine optimization steps, in sequential order, are as follows (see Figure 1).

I. Base Design Selection: The base nanocavity design is the design from which the final optimized structure will be derived. Therefore, it is important to consider which base nanocavity design has the right properties for the application in mind. For this research, the base nanocavity designs were selected for their inherent resilience to fabrication imperfections.

II. Add Fabrication Imperfections (additional step): Perturbations like surface roughness or slanted sidewalls are introduced to the simulation to mimic the effect of fabrication imperfections (see Supporting Information D1 and D2). After adding the imperfections, the optimization process is proceeded as usual. The final optimized nanocavity will have the largest *Q*-factor in the presence of these fabrication errors. It is important to note that this does not imply a higher *Q*-factor under ideal conditions. Rather, it indicates that the *Q*-factor of the optimized structure is more resilient to fabrication imperfections. Hence, this step aims to identify nanocavity structures where the *Q*-factor is better preserved in the presence of fabrication errors compared to structures optimized without considering such imperfections.

III. Data Collection: The optical properties of numerous random nanocavity designs are simulated using the FDTD method. These random nanocavity designs are derived from the base nanocavity by randomly altering specific design parameters. It is crucial to consider which parameters will be randomly varied, within what range, and according to which probability distribution, as this defines the optimization space. The defined optimization space dictates the amount of data required to effectively train a NN and the parameter space where it performs optimally.

IV. Data Preprocessing: Data preprocessing plays a crucial role in the effectiveness and efficiency of NNs.[48] First, the total data set must be divided into a training data set and a representative test data set. Second, the input and output data are transformed to improve their quality. NNs demonstrate increased stability, compatibility, and faster convergence when trained on properly scaled data that follows a normal distribution.

V. Architecture design: When designing a NN architecture, there are numerous options and techniques to consider. For

https://doi.org/10.1021/acsaom.5c00060
ACS Appl. Opt. Mater. XXXX, XXX, XXX−XXX

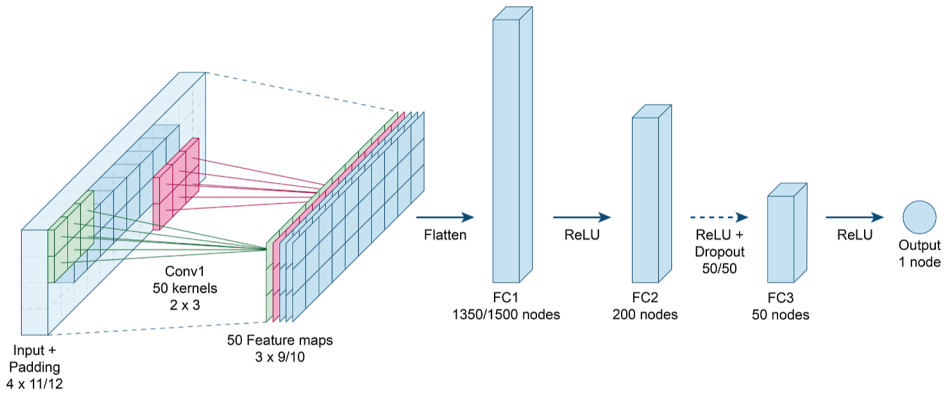

Figure 2. A schematic representation of the CNN architecture employed to optimize nanobeam cavities for fabrication error tolerance. The CNN consists of a convolutional layer followed by three FC layers, with dropout applied between the second and third FC layers to reduce overfitting. Zero-padding is applied to the input, and the ReLU activation function is utilized.[37,38]

instance, considerations include the type of NN architecture, the number of layers, the quantity of nodes per layer, activation functions, the choice of loss function, hyperparameters and the implementation of techniques such as dropout, L^2-regularization, batch normalization, and various other architectural design considerations. The specifications of the NN architecture depend on the complexity of the optimization problem at hand. A larger optimization space calls for a larger data set, a more intricate NN, and the implementation of additional techniques to mitigate computational costs and unwanted effects like overfitting or vanishing gradients.[48]

VI. Training: Throughout training, the weights and biases (internal parameters) of the NN are adjusted at the end of each loop (epoch) until the loss function is minimized. The loss function is computed by comparing the predicted optical properties, calculated with forward propagation, with the actual optical properties, computed with the FDTD method. This minimization process involves following the gradient, computed with backpropagation, in its reverse direction (gradient descent). This process continues, for a fixed amount of epochs, until the model converges to a satisfactory solution.[48]

VII. Testing: Once training is complete, the final trained model is evaluated on a separate test data set to assess its performance on unseen data. This step provides an unbiased estimate of the model's effectiveness. Afterward, the relative prediction error and correlation coefficient from the training data and test data are compared to validate the generalizability of the NN on unseen nanocavity designs.[48]

VIII. Optimization: The NN can now rapidly and accurately predict the optical properties of nanocavity designs, surpassing the computational speed of traditional methods such as the FDTD method. The goal of the optimization step is to use the trained NN to efficiently adjust design parameters, enhancing the optical properties of the base nanocavity design. This can be done with local optimization algorithms like gradient descent/ascent or global optimization algorithms like evolutionary strategies (ES). The NN, being significantly faster than the FDTD method, allows for more efficient exploration of the parameter space compared to these computationally intensive approaches.

IX. Validation: A selection of nanocavities found with the NN, exhibiting potentially superior characteristics, is subjected to validation and confirmation of their optical properties through FDTD simulation. The nanocavity design with the most favorable performance is deemed as the optimized nanocavity design.

The NN architecture used to predict the *Q*-factor of the nanobeam cavities throughout this research is a CNN with one convolutional layer, followed by a series of fully connected layers (FC). Figure 2 shows a visual representation of this CNN architecture design (step V). This NN is inspired by the work of T. Asano and S. Noda,[37,38] which employed a similar number of independent design parameters (27) and data set size (1000 nanocavities). However, unlike previous studies that focus solely on maximizing simulated *Q*-factors, this work explicitly incorporates fabrication imperfections into the optimization process, addressing a key limitation in prior approaches.[32−34,37,38,40] The CNN was chosen over an FNN due to its ability to effectively capture local spatial dependencies in nanophotonic structures, where neighboring holes strongly influence optical properties. Initial tests confirmed that a CNN outperformed an FNN in prediction accuracy and generalizability, making it the preferred architecture for this study.

The geometry of a nanobeam cavity is encoded as deviations in design parameters relative to the base nanobeam cavity. These encoded parameters are stored into a matrix that serves as input for the CNN (see Supporting Information B). The design parameters are distributed over the input matrix in such a way that the kernels of the convolutional layer can cover the relations between the geometry of neighboring unit cells. Zero-padding is applied around this matrix before passing it to the convolutional layer to ensure that information near the edges of the input matrix is also adequately processed. The optimization process involves 13 independent degrees of freedom for the L2 nanobeam cavity and 16 for the fishbone nanobeam cavity. Consequently, the input matrix, including padding, differs between the two designs: 4×11 for the L2 nanobeam and 4×12 for the fishbone nanobeam.

The convolutional layer makes use of 50 different 2×3 kernels with a stride of 1 in both directions. This results in 50 different feature maps, sized 3×9 for the L2 nanobeam cavity and 3×10 for the fishbone nanobeam cavity. These feature maps are flattened, before passed on to the first FC layer (FC1). FC1, consisting of 1350 nodes for the L2 nanobeam cavity and 1500 nodes for the fishbone nanobeam cavity, is connected to the second FC layer (FC2) through an affine transformation and a ReLU (Rectified linear unit) activation function[49] (see Supporting Information E1 and E2). FC2

https://doi.org/10.1021/acsaom.5c00060
ACS Appl. Opt. Mater. XXXX, XXX, XXX−XXX

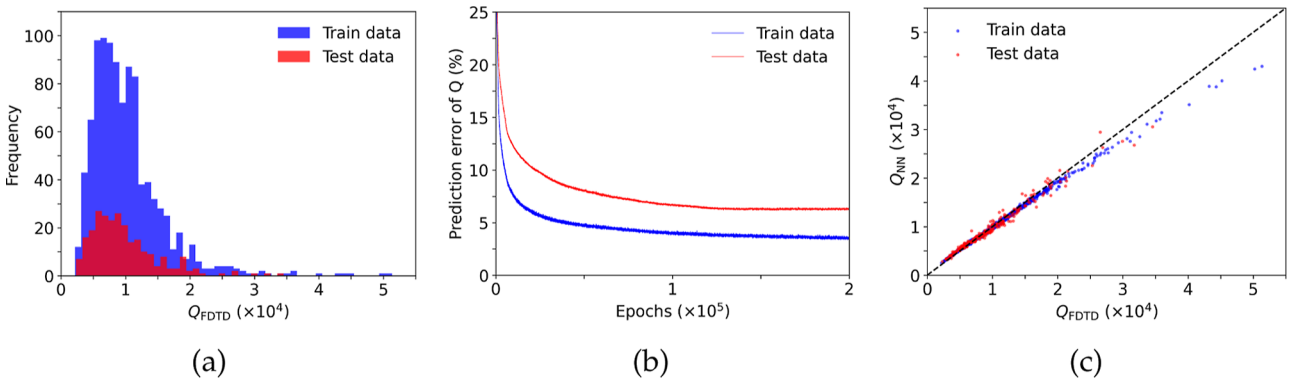

Figure 3. An overview showcasing an example of the data set, training, and correlation plots for L2 nanobeam cavities under ideal conditions, trained without L^2-regularization. Additional plots are provided in the Appendix. (a) Data set split before preprocessing. (b) Prediction error progression during training. (c) Correlation between predicted Q-factors (Q_{NN}) and simulated Q-factors (Q_{FDTD}).

consists of 200 nodes and is the same way connected to the third FC layer (FC3), but with 50/50 dropout[48] in between. FC3 has 50 nodes, and after the final affine transformations and ReLU activations, $\log_{10}(Q_{NN})$ is obtained by summing the outputs from FC3. This logarithmic transformation is part of step IV and enhances the NN's learning capabilities.[35−37,39]

The loss function of the NN is the function that will be minimized during training, by iteratively adjusting the weights and biases of the NN. The DL task addressed in this research is a regression task of a continuous variable. The default choice for such tasks is the mean-squared-error (MSE) loss function.[48] MSE is computed as the mean of the squared differences between predicted and actual values (see the first term of eq 1).

$$\begin{aligned}\text{loss} &= \text{MSE} + \text{L2} \\ &= [\log_{10}(Q_{NN}) - \log_{10}(Q_{FDTD})]^2 + \frac{1}{2}\lambda \sum_i \theta_i^2 \end{aligned} \quad (1)$$

The second term of this NN's loss function is an artificial loss term. It penalizes the use of large model parameters θ_i (weights and biases), resulting in the model learning smoother representations of the regression task and thus less overfitting. The hyperparameter λ determines the strength of the so-called L^2-regularization.[36,37] L^2-regularization is a valuable technique for preventing overfitting in DL models.[48,50] It encourages simpler models that generalize better to unseen data and prevents the memorization of noise or small fluctuations in the training data, leading to improved performance and robustness.

Numerous minimization algorithms exist with which one can minimize the loss function. In the field of DL, this minimization algorithm is referred to as the optimizer. The goal of the optimizer is to find the set of model parameters that yield the best performance on the training data while generalizing well to unseen data. For this CNN, the stochastic gradient descent (SGD) optimizer was chosen for its simplicity, efficiency, effectiveness and compatibility with the MSE loss function.[48] SGD is a widely used optimization algorithm in DL. It iteratively updates model parameters by computing the gradient of the loss function with respect to each parameter of the model.

SGD can be used in combination with adaptive learning rates. Adaptive learning techniques are algorithms that dynamically adjust the learning rate during training based on various factors such as the magnitude of gradients, the history of parameter updates, or other characteristics of the optimization landscape. For this CNN, the SGD optimizer is extended with momentum-based adaptive learning rates. Momentum helps smooth out the update trajectory and accelerate convergence by considering the history of parameter updates.[48,51] When the gradients consistently point in the same direction, momentum accumulates and amplifies the effect, leading to faster progress along the gradient descent path. Conversely, when the gradients change direction or fluctuate, momentum helps dampen the effect, reducing the impact of noisy updates and preventing the algorithm from getting stuck in local minima or saddle points.

The SGD algorithm with momentum based adaptive learning rates can be mathematically expressed as shown in eqs 2 and 3

$$\nu_n = \gamma\nu_{n-1} + \nabla_\theta L(\theta_{n-1}) \quad (2)$$

$$\theta_n = \theta_{n-1} - \alpha\nu_n \quad (3)$$

The model parameters from the previous iteration θ_{n-1} are updated by the momentum term ν_n, scaled by the learning rate hyperparameter α. This momentum term is determined by the gradient of the loss function $L(\theta_{n-1})$ with respect to the model parameters θ and the previous momentum term ν_{n-1}, scaled by the momentum hyperparameter γ. Thus, this approach takes into account the history of the parameter updates when updating the model parameters.

Additionally, various strategies exist for initializing the weights and biases of the NNs before training. For this research, the He-initialization technique is used (see Supporting Information E3).[52] After empirically studying the behavior of the NN with changes in hyperparameters, a learning rate of $\alpha = 0.001$ and a momentum of $\gamma = 0.9$ were determined to yield the optimal results. Additionally, the NNs were trained with a weight decay term of $\lambda = 0$ or $\lambda = 0.001$, allowing for the exploration of both scenarios with and without L^2-regularization.

To train the NNs, a data set containing 1250 unique nanobeam cavities is created (step III) for each base design and fabrication error implementation (including under ideal, surface roughness, and sidewall slant conditions), resulting in a total of six data sets (see Supporting Information F1). Before training, these data sets must first be preprocessed (step IV) to facilitate the efficient learning of the underlying relationships by the NNs. This involves taking the logarithm of the Q-factors and scaling the design parameters (see Supporting Information F2).

https://doi.org/10.1021/acsaom.5c00060
ACS Appl. Opt. Mater. XXXX, XXX, XXX−XXX

The total data set collected is randomly divided into a training data set and a test data set with a ratio of 8:2, resulting in 1000 training samples and 250 test samples. The splitting is done randomly to ensure that all features from the training data set are also captured in the test data set (see Figure 3a). The training process is tracked by monitoring the relative prediction error of the Q-factor. The relative prediction error is defined as shown in eq 4

$$\epsilon_{\text{pred}} = \frac{|Q_{\text{NN}} - Q_{\text{FDTD}}|}{Q_{\text{FDTD}}} \times 100\% \tag{4}$$

An example of the convergence of the training processes can be seen in Figure 3b. This graph demonstrates a rapid decrease in average prediction error during the initial 5×10^4 epochs. Thus, after 2×10^5 epochs the training process is deemed as converged. This process took approximately 150 min. Furthermore, the difference between the training and testing prediction errors serves as a measure of the model's generalizability and potential overfitting. A large difference suggests that the model performs well only on the training data and struggles to generalize effectively to new, unseen data.

Finally, the trained NNs are assessed on their ability to predict Q-factors from a given set of input design parameters. Their performance is quantified by analyzing the final relative prediction error (see eq 4) and the Pearson correlation coefficients[53] (see eq 5) between the predicted Q-factors (Q_{NN}) and the simulated Q-factors (Q_{FDTD}), for both the training and test data sets. The Pearson correlation coefficient quantifies how Q_{NN} varies in relation to Q_{FDTD}. In the ideal scenario where Q_{NN} equals Q_{FDTD}, the correlation coefficient would be 1. An example of a correlation graph is shown in Figure 3c. The covariance between Q_{NN} and Q_{FDTD} is denoted by $\text{cov}(Q_{\text{NN}}, Q_{\text{FDTD}})$, and their standard deviations are represented by σ. The Pearson correlation coefficient is defined as shown in eq 5

$$R = \frac{\text{cov}(Q_{\text{NN}}, Q_{\text{FDTD}})}{\sigma(Q_{\text{NN}})\sigma(Q_{\text{FDTD}})} \tag{5}$$

After training and testing the NNs (step VI and VII) on their predictive performance (see Supporting Information F3), the NNs can be used to efficiently optimize the nanobeam cavities (step VIII). A single FDTD simulation requires approximately 5 min to complete on an 8-core, 2.8 GHz computing cluster (see Supporting Information C). In contrast, a trained NN performs a single forward propagation in under 3×10^{-4} seconds on a single 3.49 GHz core, achieving a speed-up of more than one-million times compared to the FDTD simulation. This drastic reduction in computational time enables rapid exploration of the design space, making DL a highly efficient approach for optimizing nanobeam cavities.

To exploit this efficiency, the trained NNs are coupled with two distinct optimization algorithms: one employing a local optimization strategy and the other a global approach. Global optimization algorithms search broadly, exploring the entire solution space, while local optimization algorithms search intensively within a confined region around the initial condition. Both algorithms are deployed with a set of different hyperparameters to form a family of potentially high Q-factor nanobeam cavities (see Supporting Information G1). For this study, the best performing structure from this family is deemed as the optimized design.

The local optimization algorithm is referred to as gradient ascent (GA),[37,38] as the goal is to maximize the Q-factor by following a gradient in the design parameter landscape. Also, this way one can clearly distinguish between gradient descent, the optimizer that optimizes the weight and biases of the NN and GA, the optimization algorithm that maximizes the Q-factor by interacting with the trained NN.

$$\begin{aligned}\text{loss} &= \text{MSE} + \text{L2} \\ &= [\log_{10}(Q_{\text{NN}}) - \log_{10}(Q_{\text{t}})]^2 + \frac{1}{2}\lambda_{\text{GA}}|\vec{x} - \vec{x}_0|^2\end{aligned} \tag{6}$$

To maximize the Q-factor using the local optimization algorithm, the artificial loss function described in eq 6 is minimized. The target Q-factor is arbitrary and is set at a high value of $Q_t = 10^6$. To keep the parameter displacements $\vec{x}$ small and approximately within the initial design parameter space, an L^2-regularization term is added to the artificial loss function. This L^2-regularization is relative to the initial input structure defined by the parameter displacements $\vec{x}_0$. The gradient of the loss function with respect to $\vec{x}$ is calculated using back-propagation. The parameter displacements are then incrementally adjusted to minimize the loss, following the same principle as the SGD algorithm in optimizing the NN's loss function. Through empirical experimentation, a learning rate of $\alpha_{\text{GA}} = 10^{-5}$ and a momentum of $\gamma_{\text{GA}} = 0.9$ were selected. After 10^6 iterations, the optimization process is considered converged (see Figure S12a,b).

The global optimization algorithm used in this research belongs to the family of evolutionary strategies and is known as CMA-ES (covariance matrix adaptation evolution strategy).[32,54] As a population-based optimization approach, its population is determined through random sampling from a multivariate normal distribution. This multivariate normal distribution is updated every generation by adapting the covariance matrix and mean vector according to the elite solutions from the previous generation. These elite solutions are defined by the individuals with the highest fitness. Updating the covariance matrix in CMA-ES dynamically adjusts the algorithm's exploration strategy by learning from the performance of a subset of elite solutions. This approach enables CMA-ES to effectively explore the design parameter space and find a solution to the optimization problem.

$$\text{Fitness} = Q - \text{L2} = \log_{10}(Q_{\text{NN}}) - \frac{1}{2}\lambda_{\text{ES}}|\vec{x} - \vec{x}_0|^2 \tag{7}$$

To ensure adequate exploration of the parameter space with the global optimization algorithm, a population size of 20 is selected, with half of the population used for the adaptation of the covariance matrix. After 300 iterations, the optimization is deemed as converged (see Figure S12c,d). The fitness function, described in eq 7 and maximized by this optimization algorithm, consists of the predicted Q-factor, penalized by an L^2-regularization term. As before, this term penalizes large deviations of the parameter displacements $\vec{x}$ from the initial mean structure defined by $\vec{x}_0$. The algorithm is initialized with a multivariate normal distribution about the initial mean $\vec{x}_0$, with a initial standard deviation of $\sigma_0 = 1$.

3. RESULTS AND DISCUSSION

The two base nanobeam cavities are the elliptical-hole "L2" nanobeam cavity and the corrugated "fishbone" nanobeam cavity (see Figures 4 and 5). Both cavity designs share the

https://doi.org/10.1021/acsaom.5c00060
ACS Appl. Opt. Mater. XXXX, XXX, XXX−XXX

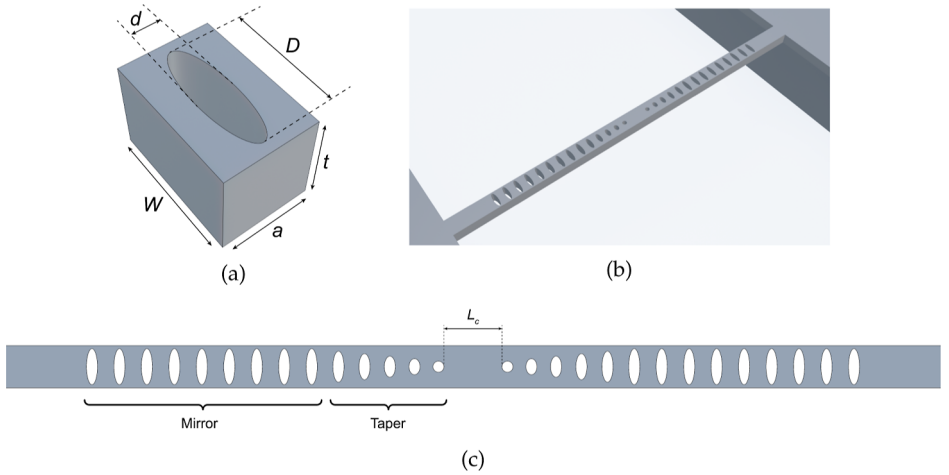

Figure 4. A visual representation of the geometric properties of the base design for the L2 nanobeam cavity. (a) A 3D model of the elliptical airhole unit cell, highlighting its key design parameters. (b) A 3D model of the complete L2 nanobeam cavity. (c) A 2D schematic of the L2 nanobeam cavity, highlighting the mirror, taper and cavity region.

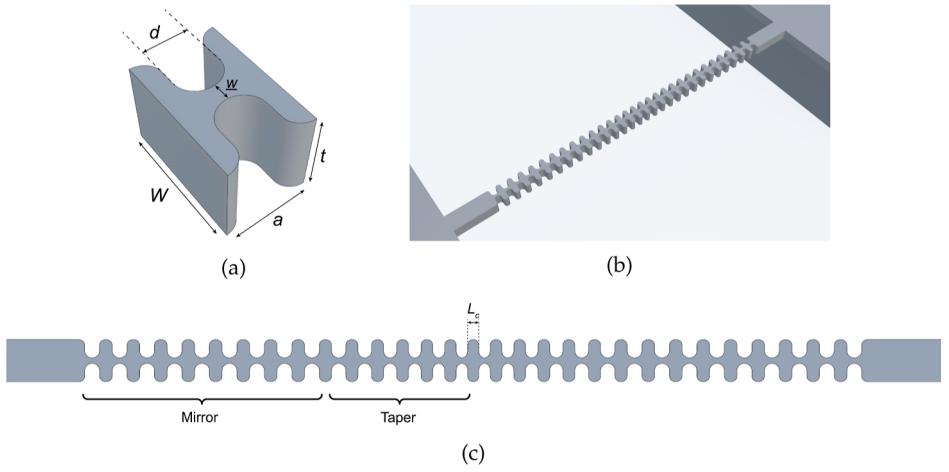

Figure 5. A visual representation of the geometric properties of the base design for the fishbone nanobeam cavity. (a) A 3D model of the corrugated unit cell, highlighting its key design parameters. (b) A 3D model of the complete fishbone nanobeam cavity. (c) A 2D schematic of the fishbone nanobeam cavity, highlighting the mirror, taper and cavity region.

same primary structural features but exhibit distinct secondary or fine features. Each cavity is integrated within an in-air-suspended diamond waveguide (n = 2.4) with a width of W = 300 nm and a thickness of t = 200 nm. To form the optical cavity, the waveguide is perturbed by airholes arranged in a 1D lattice of 30 unit cells. Both cavity geometries feature a mirror region (nine unit cells) and a taper region (six unit cells), symmetrically positioned on either side of the cavity. In the mirror region, the lattice constant is fixed at a = 195 nm. In the taper region, the spacing between the airholes, along with one other geometry are varied linearly. The spacing between the airholes is for both designs tapered from Δx = 195 − 160 nm with steps of 5 nm.

The L2 nanobeam cavity is characterized by the absence of two airholes at its center, which is why it is referred to as the L2 nanobeam cavity (see Figure 4c). The mirror region includes nine elliptical airholes, each with a minor diameter of d = 78 nm and a major diameter of D = 255 nm. The taper region consists of the innermost five airholes on each side of the cavity (or six if considering the absent airhole). The major diameter and the spacing between these airholes taper linearly from D = 255 − 78 nm and from Δx = 195 − 160 nm, respectively (accounting for the missing airhole). This results in a cavity length of L_c = 412 nm.

The fishbone nanobeam cavity is characterized by its distinctive corrugated structure, which is why it is referred to as the fishbone nanobeam cavity (see Figure 5c). Although the airholes are shaped more like grooves or channels, they will be referred to as airholes for convenience. The pairs of airholes, facing each other transversely, are separated by a spacing of $\underline{w}$ = 40 nm. Therefore, the fishbone nanobeam cavity consists of fins with a length of l = 130 nm, which are circularly rounded by arcs with a transverse diameter of D_f = 80 nm. The mirror region includes 18 airholes (nine pairs), each with a longitudinal diameter of d = 105.3 nm and transverse diameter of D_h = 100 nm. The taper region consists of the innermost 12 airholes on each side of the cavity (six pairs). The longitudinal diameter and the spacing between these airholes taper linearly from d = 105.3 − 81.3 nm and from Δx = 195 − 160 nm, respectively. This results in a cavity length of L_c = 78.7 nm.

The two distinct unit cell designs (see Figures 4a and 5a) and tapers result in different optical properties, which can be quantitatively characterized by the resonant wavelength, Q-factor, mode volume, mode distribution, and the full width at

https://doi.org/10.1021/acsaom.5c00060
ACS Appl. Opt. Mater. XXXX, XXX, XXX−XXX

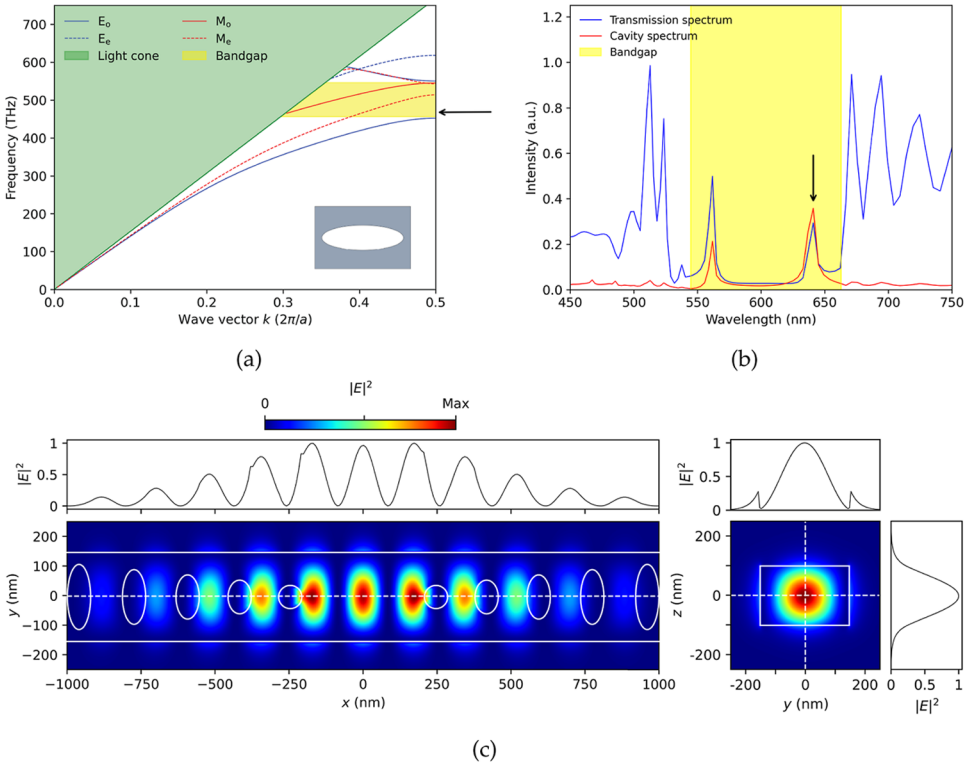

Figure 6. Optical properties of the L2 nanobeam cavity. (a) A visual representation of the band structure of the first six bands of the elliptical airhole unit cell (Rsoft BandSolve). (b) Transmission spectrum and cavity excitation spectrum plots of the L2 nanobeam cavity (Rsoft FullWave). The resonant peaks shown are not scaled to represent the actual peak intensities of the high *Q*-factors, ensuring clarity in the visualization. (c) 2D plots illustrating the mode distributions (electric field intensity $|E|^2$) of the L2 nanobeam cavity in the *xy*- and *yz*-planes, accompanied by 1D plots showing the mode distributions along the white dotted lines in the *x*-, *y*-, and *z*-directions.

half-maximum (fwhm) of the mode distribution along all three spatial directions. Graphically, these properties can be represented by the mode distribution of the electric field in the *xy*- and *yz*-planes, the optical band gaps of the two unit cell designs, and the transmission spectra combined with the cavity excitation spectra of the two nanobeam cavities (see Figures 6 and 7). For a detailed description of the numerical framework used to compute these optical properties, refer to Supporting Information C.

The base L2 nanobeam cavity design has a resonant wavelength of λ = 641 nm, with a *Q*-factor of $Q_{FDTD} = 2.4 \times 10^4$ and a mode volume of $V = 0.7\ (\lambda/n)^3$ (see Supporting Information D3 for optical properties of the base models under fabrication imperfections). The mode distribution of this resonant mode is shown in Figure 6c. The electric field distribution displays a fundamental mode profile with three peaks within the cavity, characteristic of this L2 cavity design. The $\text{fwhm}_{x,y,z}$ in all three directions are 84, 161, and 147 nm, respectively. This results in a mode that is approximately twice as spread out in the *x*-direction compared to conventional state-of-the-art nanobeam cavity designs, which typically have an fwhm_x around 40 nm.[16−22] This broader mode profile indicates that the spatial accuracy required for ion implantation in this cavity design is significantly lower.

The unit cell of the L2 nanobeam cavity (see Figure 4a) gives rise to the band structure diagram shown in Figure 6a. The band structure reveals a band gap for the E_o modes between 452 and 550 THz (545−663 nm), which are also referred to as the most TE-like modes.[12]

The transmission and cavity excitation spectra both show a resonant peak at 641 nm, marked by a black arrow in Figure 6a,b. Another resonant peak with a lower wavelength can be observed, which is typical for such airhole nanobeam cavities.[13] Finally, the band gap identified from the band structure diagram is again highlighted in yellow and approximately aligns with the band gap shown by the transmission spectrum shown in Figure 6b.

The base fishbone nanobeam cavity design has a resonant wavelength of λ = 547 nm, with a *Q*-factor of $Q_{FDTD} = 2.6 \times 10^4$ and a mode volume of $V = 1.4\ (\lambda/n)^3$ (see Supporting Information D3 for optical properties of the base models under fabrication imperfections). The mode distribution of this resonant mode is shown in Figure 7c. The electric field distribution displays a fundamental mode profile with one peak within the cavity, characteristic of this fishbone cavity design. The $\text{fwhm}_{x,y,z}$ in all three directions are 68, 194, and 130 nm, respectively. This indicates that the spatial accuracy required for ion implantation in these cavity designs is still lower compared to conventional state-of-the-art nanobeam cavity designs.[16−22]

The unit cell of the fishbone nanobeam cavity (see Figure 5a) gives rise to the band structure diagram shown in Figure 7a. The band structure again reveals a band gap for the E_o modes, this time between 579 and 519 THz (518−578 nm).[12]

The transmission and cavity excitation spectra both show a resonant peak at 547 nm, marked by a black arrow in Figure 7a,b. This is the only dominant resonant peak within the band gap. Noticeably, the resonant peak is situated more in the middle of the band gap, than with the L2 nanobeam cavity.

https://doi.org/10.1021/acsaom.5c00060
ACS Appl. Opt. Mater. XXXX, XXX, XXX−XXX

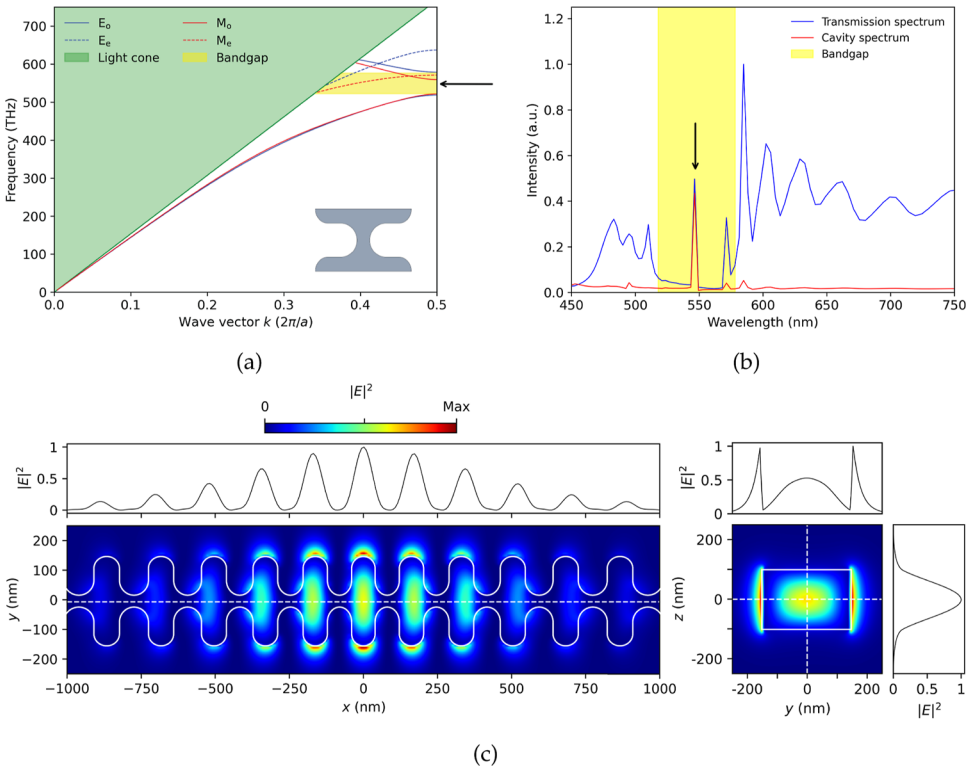

Figure 7. Optical properties of the fishbone nanobeam cavity. (a) A visual representation of the band structure of the first six bands of the corrugated unit cell (Rsoft BandSolve). (b) Transmission spectrum and cavity excitation spectrum plots of the fishbone nanobeam cavity (Rsoft FullWave). The resonant peaks depicted do not represent the actual peak intensities of the high *Q*-factors, ensuring clarity in the visualization. (c) 2D plots illustrating the mode distributions (electric field intensity $|E|^2$) of the fishbone nanobeam cavity in the *xy*- and *yz*-planes, accompanied by 1D plots showing the mode distributions along the white dotted lines in the *x*-, *y*-, and *z*-directions.

Finally, the band gap identified from the band structure diagram is again highlighted in yellow and closely aligns with the band gap shown by the transmission spectrum shown in Figure 7b.

For both the L2 and fishbone nanobeam cavities, three optimized designs are found, designated as cavity 1, cavity 2, and cavity 3 (see Supporting Information G3−G5). Cavity 1 is optimized under ideal conditions, without considering fabrication imperfections, following previous studies.[32−34,37,38] Cavity 2 is optimized to account for surface roughness and cavity 3 is designed to reduce the effects of sidewall slant. The optical characteristics of each cavity are then evaluated and compared under ideal, rough surface, and slanted sidewall conditions. These characteristics are summarized in Tables S8 and S10 for the L2 and fishbone nanobeam cavities, respectively.

Cavity 2 and cavity 3 are compared separately to cavity 1 to highlight the impact of optimizing against fabrication imperfections and to illustrate how this study extends beyond previous works that focused solely on ideal conditions. While all four cavities are included in the slant and roughness plots for completeness, the primary comparisons remain between cavity 1 and cavity 2 for their performance under surface roughness conditions, and between cavity 1 and cavity 3 for their performance under different angles of sidewall slant. The results for 100 simulated structures with varying roughness seeds are depicted using a combination of box and violin plots (see Figures 8 and S13). Also, each cavity is compared based on their performance under different angles of sidewall slant (see Figures 9 and S14). Structures are deemed more robust to fabrication imperfections if their *Q*-factor remains higher despite these imperfections and exhibits relatively less degradation from the ideal *Q*-factor. Two of the four cases are described here, with the remaining cases detailed in Supporting Information G4 and G5.

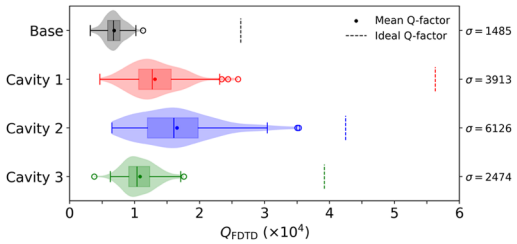

Figure 8. Box plots overlaid with violin plots show the *Q*-factor distributions for fishbone base (black), cavity 1 (red), cavity 2 (blue), and cavity 3 (green) across different surface roughness configurations. A dotted line indicates the *Q*-factor for each structure under ideal (no surface roughness) conditions. The standard deviation (σ) of each distribution is provided on the right.

The first optimized cavity evaluated is fishbone cavity 2, which is characterized by a significant reduction in the distance between opposing holes, w, compared to its base model (see Table S9). The average *Q*-factor of this structure under surface roughness, predicted by the NN, is $Q_{NN} = 1.090 \times 10^4$, while the FDTD simulation yields $Q_{FDTD} = 1.652 \times 10^4$. This results in a relative prediction error of approximately $\epsilon_{pred} = 34.02\%$ (see Table S6). This optimized design was obtained using a NN with L^2-regularization on its weights and biases (λ = 0.001) and optimized with the GA algorithm, initialized at the

https://doi.org/10.1021/acsaom.5c00060
ACS Appl. Opt. Mater. XXXX, XXX, XXX−XXX

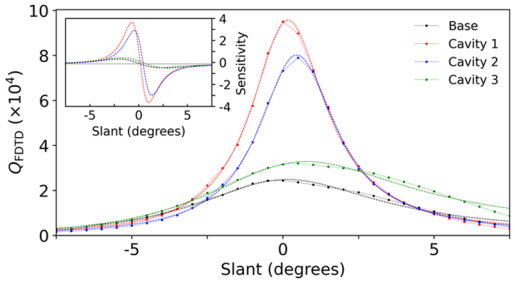

Figure 9. A graph showing the Q-factor of L2 base (black), cavity 1 (red), cavity 2 (blue), and cavity 3 (green) as a function of slant angles. The data is fitted with a linearly asymmetric Lorentzian curve, and its derivative, displayed in the inset, quantifies the sensitivity of the Q-factor to slant angle variations in units of $\times 10^4$/degree.

base design with L^2-regularization on the design parameters ($\lambda_{GA} = 0.15$).

In Figure 8, the distribution of Q-factors for the fishbone base and cavities 1, 2, and 3 is visualized across different surface roughness configurations (random seeds). Under ideal conditions (denoted by the dotted line), cavity 2 has a lower Q-factor ($Q_{ideal} = 4.247 \times 10^4$) compared to cavity 1 ($Q_{ideal} = 5.629 \times 10^4$). However, when surface roughness is applied, cavity 2 ($Q_{rough} = 1.652 \times 10^4$) outperforms cavity 1 ($Q_{rough} = 1.314 \times 10^4$) by 25.72% on average. As a result, under surface roughness, cavity 2 demonstrates improved performance and experiences a 15.55% smaller average degradation compared to cavity 1, making it more robust against the fabrication imperfection of surface roughness. Although cavity 2 shows higher sensitivity to variations in roughness configurations (evidenced by its larger standard deviation), it has a high probability of outperforming cavity 1 under surface roughness conditions.

The second optimized cavity evaluated is L2 cavity 3, which is characterized by a shift of all holes toward the cavity (see Table S7). The Q-factor of this structure under 5° sidewall slant, predicted by the NN, is $Q_{NN} = 1.607 \times 10^4$, while the FDTD simulation yields $Q_{FDTD} = 1.962 \times 10^4$. This results in a relative prediction error of approximately $\epsilon_{pred} = 18.09\%$ (see Table S6). This optimized design was obtained using a NN without L^2-regularization on its weights and biases ($\lambda = 0$) and optimized with the CMA-ES algorithm, initialized at the best structure of the training data with L^2-regularization on the design parameters ($\lambda_{ES} = 0.15$).

In Figure 9, the Q-factors of the L2 base and cavities 1, 2, and 3 are compared across varying angles of sidewall slant. Despite cavity 3 initially having a lower Q-factor ($Q_{ideal} = 3.155 \times 10^4$) compared to cavity 1 ($Q_{ideal} = 9.504 \times 10^4$) under 0° slant, it begins to outperform cavity 1 at slant angles exceeding 2.5° and performs comparably for slant angles below −2.5°. Cavity 3 was specifically optimized against a 5° slant. At this angle, the Q-factor of cavity 1 degrades to $Q_{slant} = 9404$, while cavity 3 maintains a higher Q-factor of $Q_{slant} = 1.962 \times 10^4$. As a result, under sidewall slant, cavity 3 achieves more than twice the performance of cavity 1 and experiences 52.28% less degradation, making it more robust against the fabrication imperfection of sidewall slant. Additionally, the inset of Figure 9 reveals that cavity 3 is significantly less sensitive to sidewall slant variations than cavity 1 for angles beyond −2.5°.

The NN-driven optimization technique incorporated from previous studies[32−34,37,38] consistently produced structures with significantly higher Q-factors than the original base models, achieving up to a 5× improvement over the initial Q-factor. Building on these advancements, our approach extends these methodologies by explicitly incorporating fabrication imperfections into the optimization process. This inclusion proved effective, yielding more robust device designs that are better suited for real-world conditions.

However, some patterns and complications emerged. For instance, the fishbone nanobeam cavity, despite its initially higher Q-factor, showed less improvement under ideal fabrication conditions compared to the L2 nanobeam cavity. This difference may stem from the NNs performing less effectively on the fishbone cavity due to differences in the parameters and the size of the optimization space (see Tables S1 and S2). Additionally, it is plausible that the fishbone cavity's optimization space offers lower maxima, indicating inherently less potential for improvement compared to the L2 cavity.

The design parameters of the optimized structures largely remained within the initial data set's range (see Tables S7 and S9). This limitation arises from the NNs' degrading performance outside their training parameter space, leaving a large portion of the entire parameter space unexplored.

In addition, the NNs struggled to predict high Q-factors, with the lowest prediction error for the optimized designs being $\epsilon_{pred} = 18.09\%$ (see Table S6). Notably, NNs with L^2-regularization faced the greatest difficulty in accurately predicting high Q-factors, consistently underestimating them (see Figure S10). This underprediction is attributed to the lack of high-Q training data. Despite this limitation, the NNs were successful in identifying peaks in the optimization landscape, accurately evaluating the gradient direction of Q-factors with respect to the design parameters. The iterative optimization approach[32,33,38,40] addresses the challenge of limited high-Q data and inefficient parameter space exploration. By training NNs on data beyond the initial parameter space, this method provides high-Q training data after the first iteration, enabling the exploration of higher Q-factors and more fabrication error-tolerant devices.

While the NN-driven optimization technique has demonstrated significant improvements in Q-factors and robustness to common fabrication imperfections, transitioning from simulation-based optimization to practical nanofabrication and experimental validation presents several challenges. These simulations will inevitably still rely on idealized assumptions, such as perfect material properties, uniform geometries (e.g., thickness, width, and hole dimensions), and optimal boundary conditions (e.g., symmetry constraints). Additionally, process fluctuations in nanofabrication, leading to batch-to-batch and device-to-device variability, further complicate both characterization and the comparison with simulations. Advancements in hybrid methodologies—incorporating feedback loops from experimental data—along with high-resolution characterization and precise process control, will be essential to ensure a seamless and effective transition of optimized designs to real-world conditions.

4. CONCLUSIONS

Diamond's exceptional material properties cause unavoidable fabrication imperfections that degrade photonic device performances. This research focuses on counteracting the affects of such structural imperfections through design optimizations and advances scalable quantum photonic hardware by introducing an effective design methodology for

https://doi.org/10.1021/acsaom.5c00060
ACS Appl. Opt. Mater. XXXX, XXX, XXX−XXX

fabrication-tolerant PhC nanobeam cavities, enabling on-chip diamond quantum systems.

The considered fabrication imperfections include surface roughness, sidewall slant, and nonoptimal emitter positioning. Two nanobeam cavity designs were optimized: one with elliptical holes and one with a corrugated structure. These designs were selected for their potential to enhance fabrication tolerance by providing large cavity regions that improve spatial-spectral coupling between the emitter and resonant mode and reduce noise from nearby surface charge variations, thereby maintaining high performance even under nonideal conditions.

The optimization of the two nanobeam cavity designs utilized DL, replacing FDTD simulations with CNNs trained on both ideal and realistic fabrication conditions. By incorporating imperfections into the training data, the NNs learned to produce designs that perform well even under real-world conditions. These models predict Q-factors for nanobeam cavities based on the two base designs with prediction errors as low as 3.99% and correlation coefficients up to 0.988, while operating over one-million times faster than FDTD simulations. This substantial speed-up allows for efficient exploration and optimization across large parameter spaces, enabling the discovery of robust, high-performing designs that would otherwise be computationally unattainable.

The two nanobeam cavity designs were optimized under three conditions: ideal, surface roughness, and sidewall slant. This process resulted in six distinct optimized designs. When tested against fabrication imperfections, nearly all four real-world-optimized designs demonstrated better performance and significantly less degradation compared to the two ideal-world-optimized designs. These results confirm that optimizing for fabrication imperfections using this DL-based approach produces more robust devices. Furthermore, this study demonstrates that fabrication challenges can be addressed through design optimization rather than relying solely on fabrication process optimization and most importantly that optimizing for extremely high Q-factors may not always yield the best overall device performance, especially when dealing with such fabrication imperfections.

While effective, the current DL approach faces limitations in handling extremely high Q-factors. Future work could address these challenges by iteratively expanding the data set with high-Q candidates validated through FDTD simulations and by improving NN architectures for better performance, such as through enhanced regularization, hyperparameter optimization, or exploring alternative architectures like transformers or RL-based models.

However, the most critical next step is realizing these optimized structures through nanofabrication. Testing the performance of both the ideal-world-optimized and real-world-optimized designs will provide valuable insights into the actual improvements in device robustness achieved by this approach. Ultimately, integrating this optimization strategy with active fabrication processes could further enhance device reliability by directly addressing the fabrication imperfections dealt with during manufacturing.

In conclusion, this research provides an important stepping stone for the scalable integration of color centers in diamond for quantum information processing and highlights the potential of design-based optimization to overcome fabrication challenges in nanophotonic devices. It shows that robust, high-performance devices can be achieved even under less-than-ideal manufacturing conditions. Looking ahead, this design optimization strategy can be expanded to a wider range of quantum systems, paving the way for more resilient and scalable quantum technologies that can withstand the inherent imperfections of real-world fabrication processes.

■ ASSOCIATED CONTENT

Supporting Information

The Supporting Information is available free of charge at https://pubs.acs.org/doi/10.1021/acsaom.5c00060.

> Deep learning-optimized, fabrication error-tolerant photonic crystal nanobeam cavities for scalable on-chip diamond quantum systems. (A) Explanation of resonant optical trapping in optical cavities, the definitions of Q-factor and mode volume, and their role in enhancing spontaneous emission through Purcell enhancement to improve spin-photon entanglement in color centers. (B) Optimization space for structural design parameters of L2 and fishbone nanobeam cavities, including parameter selection, variation ranges, and encoding into input matrices for CNN-based analysis. (C) Simulation framework for cavity analysis using Rsoft's FullWAVE and BandSOLVE, detailing simulation parameters, boundary conditions, and computational setup. (D) A detailed description of the implemented fabrication imperfections, namely surface roughness and sidewall slant, and an evaluation of their impact on the performance of the base nanobeam cavities, focusing on changes in Q-factor, mode volume, and resonant wavelength. (E) Further details on the CNN architecture, focusing on the affine transformation, activation function, and model initialization, which, together with the loss function, optimizer, and node configuration, define how the network processes input data and learns effectively. (F) Data set generation, preprocessing, and an examination of model performance, highlighting the impact of the implemented fabrication imperfections and L^2-regularization on NN prediction accuracy and generalization. (G) Optimization with the trained NNs, description of the family of candidate structures, examination of the optimization process, overview of the design parameter displacements of the six optimized designs, and the remaining results for the L2 nanobeam cavity under surface roughness and the fishbone nanobeam cavity under sidewall slant. Appendix: All data sets graphically presented to highlight the data split and preprocessing, along with the training process and correlation graphs for the L2 and fishbone nanobeam cavities under real-world, surface roughness, and sidewall slant conditions (PDF)

■ AUTHOR INFORMATION

Corresponding Author

Sander van Haagen − *Department of Applied Sciences and QuTech, Delft University of Technology, Delft 2628 CJ, Netherlands; Department of Quantum & Computer Engineering, Delft University of Technology, Delft 2628 CD, Netherlands;* orcid.org/0009-0002-3816-2008; Email: svhaagen@gmail.com

https://doi.org/10.1021/acsaom.5c00060
ACS Appl. Opt. Mater. XXXX, XXX, XXX−XXX

Authors

Salahuddin Nur − *Department of Quantum & Computer Engineering, Delft University of Technology, Delft 2628 CD, Netherlands*

Ryoichi Ishihara − *Department of Quantum & Computer Engineering, Delft University of Technology, Delft 2628 CD, Netherlands; QuTech, Delft University of Technology, Delft 2628 CJ, Netherlands*

Complete contact information is available at: https://pubs.acs.org/10.1021/acsaom.5c00060

Notes

The authors declare no competing financial interest.

■ ACKNOWLEDGMENTS

The authors thank Ir. M. van Beusekom (Q&CE) for essential IT support and Dr. E. Akiki (RSoft) for assistance with the simulation software. They also appreciate insightful discussions with Asst. Prof. E. Greplová.

■ REFERENCES

(1) Ishihara, R.; Hermias, J.; Yu, S.; Yu, K. Y.; Li, Y.; Nur, S.; Iwai, T.; Miyatake, T.; Kawaguchi, K.; Doi, Y.; Sato, S. 3D Integration Technology for Quantum Computer based on Diamond Spin Qubits. *2021 IEEE International Electron Devices Meeting (IEDM)*; IEEE, 2021, pp 14 5 1−14 5 4.

(2) Degen, C. L.; Reinhard, F.; Cappellaro, P. Quantum sensing. *Rev. Mod. Phys.* **2017**, *89*, 035002.

(3) Ruf, M.; Wan, N. H.; Choi, H.; Englund, D.; Hanson, R. Quantum networks based on color centers in diamond. *J. Appl. Phys.* **2021**, *130*, 070901.

(4) Van der Sar, T. Quantum Control of Single Spins and Single Photons in Diamond. Ph.D. Thesis, TU Delft, 2012.

(5) Michaels, C. Group-IV Colour Centres in Diamond for Multi-Photon Entangled State Generation. Ph.D. Thesis, Cambridge U., 2023.

(6) Rugar, A. E. Quantum Photonics With the Tin-vacancy Center in Diamond. Ph.D. Thesis, Stanford University, 2022.

(7) Debroux, R. Developing the Spin Qubit of the Tin-vacancy Center in Diamond for Quantum Networks. Ph.D. Thesis. Apollo—University of Cambridge Repository, 2022.

(8) Bernien, H.; Hensen, B.; Pfaff, W.; Koolstra, G.; Blok, M. S.; Robledo, L.; Taminiau, T. H.; Markham, M.; Twitchen, D. J.; Childress, L.; et al. Heralded entanglement between solid-state qubits separated by three metres. *Nature* **2013**, *497*, 86−90.

(9) Janitz, E.; Bhaskar, M. K.; Childress, L. Cavity quantum electrodynamics with color centers in diamond. *Optica* **2020**, *7*, 1232−1252.

(10) Bradac, C.; Gao, W.; Forneris, J.; Trusheim, M. E.; Aharonovich, I. Quantum nanophotonics with group IV defects in diamond. *Nat. Commun.* **2019**, *10*, 5625.

(11) Fox, A. M. *Quantum Optics: An Introduction*; Oxford University Press, 2006; Vol. *15*.

(12) Joannopoulos, J. D.; Johnson, S. G.; Winn, J. N.; Meade, R. D. *Photonic Crystals: Molding the Flow of Light*, 2nd ed.; Princeton University Press, 2008.

(13) Md Zain, A. R. One-dimensional Photonic Crystal/Photonic Wire Cavities Based on Silicon-on-insulator (SOI). Ph.D. Thesis, University of Glasgow, 2009.

(14) Bhaskar, M. K.; Riedinger, R.; Machielse, B.; Levonian, D. S.; Nguyen, C. T.; Knall, E. N.; Park, H.; Englund, D.; Lončar, M.; Sukachev, D. D.; et al. Experimental demonstration of memory-enhanced quantum communication. *Nature* **2020**, *580*, 60−64.

(15) Nguyen, C.; Sukachev, D.; Bhaskar, M.; Machielse, B.; Levonian, D.; Knall, E.; Stroganov, P.; Chia, C.; Burek, M.; Riedinger, R.; et al. An integrated nanophotonic quantum register based on silicon-vacancy spins in diamond. *Phys. Rev. B* **2019**, *100*, 165428.

(16) Pregnolato, T.; Stucki, M. E.; Bopp, J. M.; v d Hoeven, M. H.; Gokhale, A.; Krüger, O.; Schröder, T. Fabrication of Sawfish photonic crystal cavities in bulk diamond. *APL Photonics* **2024**, *9*, 036105.

(17) Kuruma, K.; Pingault, B.; Chia, C.; Renaud, D.; Hoffmann, P.; Iwamoto, S.; Ronning, C.; Lončar, M. Coupling of a single tin-vacancy center to a photonic crystal cavity in diamond. *Appl. Phys. Lett.* **2021**, *118*, 230601.

(18) Rugar, A. E.; Aghaeimeibodi, S.; Riedel, D.; Dory, C.; Lu, H.; McQuade, P. J.; Shen, Z.-X.; Melosh, N. A.; Vučković, J. Quantum photonic interface for tin-vacancy centers in diamond. *Phys. Rev. X* **2021**, *11*, 031021.

(19) Mouradian, S.; Wan, N. H.; Schröder, T.; Englund, D. Rectangular photonic crystal nanobeam cavities in −bulk diamond. *Appl. Phys. Lett.* **2017**, *111*, 021103.

(20) Ding, S. W.; Haas, M.; Guo, X.; Kuruma, K.; Jin, C.; Li, Z.; Awschalom, D. D.; Delegan, N.; Heremans, F. J.; High, A.; Loncar, M. High-Q Cavity Interface for Color Centers in Thin Film Diamond. *Nat. Commun.* **2024**, *15*, 6358.

(21) Regan, B.; Trycz, A.; Fröch, J. E.; Schaeper, O. C.; Kim, S.; Aharonovich, I. Nanofabrication of high Q, transferable diamond resonators. *Nanoscale* **2021**, *13*, 8848−8854.

(22) Lee, J. C.; Bracher, D. O.; Cui, S.; Ohno, K.; McLellan, C. A.; Zhang, X.; Andrich, P.; Alemán, B.; Russell, K. J.; Magyar, A. P.; et al. Deterministic coupling of delta-doped nitrogen vacancy centers to a nanobeam photonic crystal cavity. *Appl. Phys. Lett.* **2014**, *105*, 261101.

(23) Jung, T.; Görlitz, J.; Kambs, B.; Pauly, C.; Raatz, N.; Nelz, R.; Neu, E.; Edmonds, A. M.; Markham, M.; Mücklich, F.; et al. Spin measurements of NV centers coupled to a photonic crystal cavity. *APL Photonics* **2019**, *4*, 120803.

(24) Osgood, R., Jr.; Meng, X. *Principles of Photonic Integrated Circuits*; Springer, 2021.

(25) Nakamura, T.; Takahashi, Y.; Tanaka, Y.; Asano, T.; Noda, S. Improvement in the quality factors for photonic crystal nanocavities via visualization of the leaky components. *Opt. Express* **2016**, *24*, 9541−9549.

(26) Maeno, K.; Takahashi, Y.; Nakamura, T.; Asano, T.; Noda, S. Analysis of high-Q photonic crystal L3 nanocavities designed by visualization of the leaky components. *Opt. Express* **2017**, *25*, 367−376.

(27) Akahane, Y.; Asano, T.; Song, B.-S.; Noda, S. High-Q photonic nanocavity in a two-dimensional photonic crystal. *nature* **2003**, *425*, 944−947.

(28) Song, B.-S.; Noda, S.; Asano, T.; Akahane, Y. Ultra-high-Q photonic double-heterostructure nanocavity. *Nat. Mater.* **2005**, *4*, 207−210.

(29) Tanaka, Y.; Asano, T.; Noda, S. Design of Photonic Crystal Nanocavity With Q-Factor of ∼ 109. *J. Lightwave Technol.* **2008**, *26*, 1532−1539.

(30) Lai, Y.; Pirotta, S.; Urbinati, G.; Gerace, D.; Minkov, M.; Savona, V.; Badolato, A.; Galli, M. Genetically designed L3 photonic crystal nanocavities with measured quality factor exceeding one million. *Appl. Phys. Lett.* **2014**, *104*, 241101.

(31) Minkov, M.; Savona, V. Automated optimization of photonic crystal slab cavities. *Sci. Rep.* **2014**, *4*, 5124.

(32) Takahashi, K.; Baba, T. Optimization of a photonic crystal nanocavity using covariance matrix adaptation evolution strategy. *IEEE Photonics J.* **2022**, *14*, 1−5.

(33) Abe, R.; Takeda, T.; Shiratori, R.; Shirakawa, S.; Saito, S.; Baba, T. Optimization of an H0 photonic crystal nanocavity using machine learning. *Opt. Lett.* **2020**, *45*, 319−322.

(34) Liu, L.; Ma, C.; Ye, M.; Yu, Z.; Xue, W.; Hu, Z.; Li, J. Photonic crystal nanobeam cavity with a high experimental Q factor exceeding two million based on machine learning. *J. Lightwave Technol.* **2022**, *40*, 7150−7158.

(35) Li, R.; Gu, X.; Li, K.; Huang, Y.; Li, Z.; Zhang, Z. Deep learning-based modeling of photonic crystal nanocavities. *Opt. Mater. Express* **2021**, *11*, 2122−2133.

(36) Li, R.; Gu, X.; Shen, Y.; Li, K.; Li, Z.; Zhang, Z. Smart and rapid design of nanophotonic structures by an adaptive and regularized deep neural network. *Nanomaterials* **2022**, *12*, 1372.
(37) Asano, T.; Noda, S. Optimization of photonic crystal nanocavities based on deep learning. *Opt. Express* **2018**, *26*, 32704−32717.
(38) Asano, T.; Noda, S. Iterative optimization of photonic crystal nanocavity designs by using deep neural networks. *Nanophotonics* **2019**, *8*, 2243−2256.
(39) Chen, X.; Li, R.; Yu, Y.; Shen, Y.; Li, W.; Zhang, Y.; Zhang, Z. POViT: vision transformer for multi-objective design and characterization of photonic crystal nanocavities. *Nanomaterials* **2022**, *12*, 4401.
(40) Li, R.; Zhang, C.; Xie, W.; Gong, Y.; Ding, F.; Dai, H.; Chen, Z.; Yin, F.; Zhang, Z. Deep reinforcement learning empowers automated inverse design and optimization of photonic crystals for nanoscale laser cavities. *Nanophotonics* **2023**, *12*, 319−334.
(41) Wiecha, P. R.; Arbouet, A.; Girard, C.; Muskens, O. L. Deep learning in nano-photonics: inverse design and beyond. *Photon. Res.* **2021**, *9*, B182−B200.
(42) Ma, W.; Liu, Z.; Kudyshev, Z. A.; Boltasseva, A.; Cai, W.; Liu, Y. Deep learning for the design of photonic structures. *Nat. Photonics* **2021**, *15*, 77−90.
(43) Pacheco, J.; Singh, M.; Perry, D.; Wendt, J.; Ten Eyck, G.; Manginell, R.; Pluym, T.; Luhman, D.; Lilly, M.; Carroll, M.; et al. Ion implantation for deterministic single atom devices. *Rev. Sci. Instrum.* **2017**, *88*, 123301.
(44) Groot-Berning, K.; Jacob, G.; Osterkamp, C.; Jelezko, F.; Schmidt-Kaler, F. Fabrication of 15NV- centers in diamond using a deterministic single ion implanter. *New J. Phys.* **2021**, *23*, 063067.
(45) Asano, T.; Song, B.-S.; Noda, S. Analysis of the experimental Q factors (∼ 1 million) of photonic crystal nanocavities. *Opt. Express* **2006**, *14*, 1996−2002.
(46) Li, W.; Bulla, D.; Love, J.; Luther-Davies, B.; Charles, C.; Boswell, R. Deep dry-etch of silica in a helicon plasma etcher for optical waveguide fabrication. *J. Vac. Sci. Technol., A* **2005**, *23*, 146−150.
(47) Bopp, J. M.; Plock, M.; Turan, T.; Pieplow, G.; Burger, S.; Schröder, T. Sawfish'Photonic Crystal Cavity for Near-Unity Emitter-to-Fiber Interfacing in Quantum Network Applications. *Adv. Opt. Mater.* **2023**, *12*, 2301286.
(48) Bengio, Y.; Goodfellow, I.; Courville, A. *Deep Learning*; MIT Press: Cambridge, MA, USA, 2017; Vol. *1*.
(49) Sharma, S.; Sharma, S.; Athaiya, A. Activation functions in neural networks. *Towards Data Sci.* **2020**, *04*, 310−316.
(50) Girosi, F.; Jones, M.; Poggio, T. Regularization theory and neural networks architectures. *Neural Comput.* **1995**, *7*, 219−269.
(51) Sutskever, I.; Martens, J.; Dahl, G.; Hinton, G. On the importance of initialization and momentum in deep learning *International Conference on Machine Learning*; PMLR, 2013, pp 1139−1147.
(52) He, K.; Zhang, X.; Ren, S.; Sun, J. Delving deep into rectifiers: Surpassing human-level performance on imagenet classification *Proceedings of the IEEE International Conference on Computer Vision*; IEEE, 2015, pp 1026−1034.
(53) Cohen, I.; Huang, Y.; Chen, J.; Benesty, J.; Benesty, J.; Chen, J.; Huang, Y.; Cohen, I. Pearson correlation coefficient. *Noise Reduction in Speech Processing*; Springer, 2009; pp 1−4.
(54) Hansen, N.; Ostermeier, A. Completely derandomized self-adaptation in evolution strategies. *Evol. Comput.* **2001**, *9*, 159−195.

https://doi.org/10.1021/acsaom.5c00060
ACS Appl. Opt. Mater. XXXX, XXX, XXX−XXX